remote sensing

MDPI

Article

Validation of MODIS Temperature and Emissivity Products Based on Ground-Based Mid-Wave Hyperspectral Imaging Measurement in the Northwestern Plateau Region of Qinghai, China

Yuepeng Jiang, Yunhua Cao *, Zhensen Wu and Yisen Cao

School of Physics, Xidian University, Xi'an 710071, China; 21051212165@stu.xidian.edu.cn (Y.J.); wuzhs@mail.xidian.edu.cn (Z.W.); yscao@xidian.stu.edu.cn (Y.C.)
* Correspondence: yhcao@mail.xidian.edu.cn

Abstract: The climatic fluctuations in northern China exhibit remarkable variability, making it imperative to harness the power of MODIS data for conducting comprehensive investigations into the influences of desertification, desert expansion, and snow and ice melting phenomena. Consequently, the rigorous evaluation of MODIS land surface temperature (LST) and land surface emissivity (LSE) products takes on a momentous role, as this provides an essential means to ensure data accuracy, thereby instilling confidence in the robustness of scientific analyses. In this study, a high-resolution hyperspectral imaging instrument was utilized to measure mid-wave hyperspectral images of grasslands and deserts in the northwest plateau region of Qinghai, China. The measured data were processed in order to remove the effects of sensor noise, atmospheric radiation, transmission attenuation, and scattering caused by sunlight and atmospheric radiation. Inversion of the temperature field and spectral emissivity was performed on the measured data. The inverted data were compared and validated against MODIS land surface temperature and emissivity products. The validation results showed that the absolute errors of emissivity of grassland backgrounds provided by MCD11C1 in the three mid-wave infrared bands (3.66–3.840 μm, 3.929–3.989 μm, and 4.010–4.080 μm) were 0.0376, 0.0191, and 0.0429, with relative errors of 3.9%, 2.1%, and 4.8%, respectively. For desert backgrounds, the absolute errors of emissivity were 0.0057, 0.0458, and 0.0412, with relative errors of 0.4%, 4.9%, and 3.9%, respectively. The relative errors for each channel were all within 5%. Regarding the temperature data products, compared to the inverted temperatures of the deserts and grasslands, the remote sensing temperatures provided by MOD11L2 had absolute errors of ±2.3 K and ±4.1 K, with relative errors of 1.4% and 0.7%, respectively. The relative errors for the temperature products were all within 2%.

Keywords: mid-wave infrared; hyperspectral imaging; MODIS; LST inversion; LSE inversion

Citation: Jiang, Y.; Cao, Y.; Wu, Z.; Cao, Y. Validation of MODIS Temperature and Emissivity Products Based on Ground-Based Mid-Wave Hyperspectral Imaging Measurement in the Northwestern Plateau Region of Qinghai, China. *Remote Sens.* **2023**, *15*, 3893. https://doi.org/10.3390/rs15153893

Academic Editor: Ernesto López-Baeza

Received: 6 June 2023
Revised: 20 July 2023
Accepted: 3 August 2023
Published: 6 August 2023

1. Introduction

MODIS is a detector mounted on the Terra and Aqua satellites, part of the Earth Observing System (EOS) developed by the National Aeronautics and Space Administration (NASA) of the United States. It operates in a sun-synchronous orbit and offers high temporal and spectral resolution along with the advantage of global free access [1]. MODIS remote sensing technology has become an important means of obtaining regional-scale, hourly land surface temperature [2–4], and emissivity data [5,6]. It provides up to 41 products, among which emissivity and land surface temperature products play a crucial role in ecological environment monitoring [7], agricultural remote sensing, forest fire monitoring, climate studies, weather forecasting, and land model assimilation. They are particularly important for estimating sensible and latent heat fluxes and studying surface energy balance [8]. The climate in northern China varies significantly. Long-term remote sensing data can be used to study the impacts of desertification, gain further understanding of desertification

prevention and control efforts, and examine climate change mechanisms [8]. However, the issue of uncertainty in retrieving LST and emissivity from satellite measurements has been a long-standing challenge [9]. In regions like the northwestern plateau of China, which has vast territories and diverse climates, studying LST and emissivity products holds special importance [10].

In their research on the validation of MODIS data, Erb et al. evaluated Landsat-8 albedo products across polar regions by combining the BRDF kernel weights provided by MODIS. The products were extensively validated under different land cover and conditions, demonstrating their effectiveness in capturing transient, heterogeneous, and dynamic surface conditions at the landscape scale in polar regions [11]. Glynn C. Hulley used the Temperature Emissivity Separation (TES) algorithm to validate and assess the accuracy of the MXD21/VNP21 products [12]. Karina H. Zikan validated MODIS LST (MOD/MYD2017 C17 strip-level products) using temperature data from 2014 sites of the Programme for Monitoring of the Greenland Ice Sheet (PROMICE). The results showed significant differences between the LST products and the measured temperature data, especially at 0 °C, with an RMSE of 3.2K [13]. H. Fréville compared MODIS temperature products in Antarctica with hourly ground-measured surface temperature data collected at seven sites from the Baseline Surface Radiation Network (BSRN) and automatic weather stations (AWSs) throughout 2009. The temperature errors ranged from 2.2 K to 4.8 K in Antarctica [14]. GC Hulley compared the fourth and fifth versions of MODIS long-wave infrared emissivity products and validated them against experimental measurements of sand samples from the Namib Desert, revealing average relative errors of 1.06%, 0.65%, and 1.93% at 8.55 µm, 11 µm, and 12 µm, respectively [15].

However, most studies on MODIS remote sensing data are limited by experimental measurement conditions [16]. State-of-the-art validation experiments are primarily conducted using spectrometers and thermal imagers [10,17,18], which results in the separation of the spatial and spectral information of the targets. In the context of hyperspectral imaging data, due to the scarcity of instrument equipment, research efforts have mainly focused on the visible/near-infrared [19–22] and long-wave infrared regions [23,24], with less emphasis being placed on the emissivity and temperature products in the mid-wave (3–5 µm) range of MODIS. Furthermore, compared to non-imaging spectrometers, Mid-wave infrared hyperspectral images typically exhibit higher noise levels, and previous studies have shown that measurement noise significantly affects the final emissivity inversion [25–27]. However, so far, few studies have considered the noise issue in the validation process of mid-wave infrared hyperspectral imagers for MODIS emissivity and temperature products. In the data processing stage, it was observed that the mid-wave infrared was more susceptible to atmospheric system radiation and sunlight scattering compared to the long-wave infrared [28], resulting in a decrease in the accuracy of the inversion. In terms of the validation of MODIS products for emissivity and temperature, only a few studies have taken into account the anisotropic effect of the land surface in removing scattering components.

In this study, we conducted experimental measurements of typical land surface backgrounds in the northwestern plateau region of China using the Hyper-Cam mid-wave hyperspectral imaging instrument developed by TELOPS [28]. In terms of data preprocessing, equivalent noise estimation and Gaussian filtering were applied to the experimental data for denoising. Subsequently, in order to accurately interpret the data collected by the sensors, it was important to consider the impact of the Earth's atmosphere on the measured electromagnetic waves. The atmosphere interacts with these waves through absorption, scattering, and emission processes, thereby modifying the signals received by the sensors. In order to account for these atmospheric effects, a process known as atmospheric correction is necessary. In our study, we employed MODTRAN 4.0, which is widely recognized for its accuracy in simulating atmospheric radiation and transmission attenuation. We calculated the atmospheric transmission parameters specific to our measurement location. By applying these parameters, we were able to perform an effective atmospheric correction on the measured data. This correction process removed the influence of atmo-

spheric factors and allowed for a more accurate analysis and interpretation of the collected data. Finally, by combining the MCD43C1 product of MODIS with the solar radiance and sky background radiation calculated by MODTRAN 4.0, the influence of target scattering from the sun and atmospheric backgrounds was eliminated. Considering the scale effects between satellite data and measured data, a point-to-area scaling conversion method was employed to extract temperature and emissivity based on the measured data, which were then compared with MODIS temperature and emissivity products' for validation.

2. Materials and Methods

2.1. Study Area

The study area is situated in the northwestern plateau of Qinghai, China, with a latitude range of 37.375° to 38.075°N and a longitude range of 95.075° to 95.975°E. This region experiences a typical plateau continental climate, characterized by intense solar radiation, long sunshine duration, and significant diurnal temperature variations. The elevation in the study area spans approximately 2790 m to 5390 m. Contour maps play a crucial role in providing information about the terrain's elevation, aiding our understanding and simulation of the vertical distribution of the atmosphere. In the context of atmospheric correction, contour maps are valuable for estimating parameters like optical thickness, aerosol content, and water vapor content. By incorporating these parameters, a more precise calculation of the atmospheric transmission and scattering effects on measurement data can be achieved. Topographic contour data of the study area were sourced from the National Standard Database of the National Geomatics Center of China. Figure 1 presents an illustration of the contour map depicting the study area's topography and elevation.

A land cover distribution map of the study area was obtained using the MCD12 product data from MODIS remote sensing, as shown in Figure 2. According to the classification system of the International Geosphere-Biosphere Programme (IGBP) for land cover types [29] (see Table 1), the land cover in the region is primarily composed of 94.76% barren land (desert), 2.06% grassland, 1.14% permanent snow and ice, 1.38% cropland, and other types of land cover. For this study, we selected two representative natural land cover types in the northwestern region: grassland and desert (barren land).

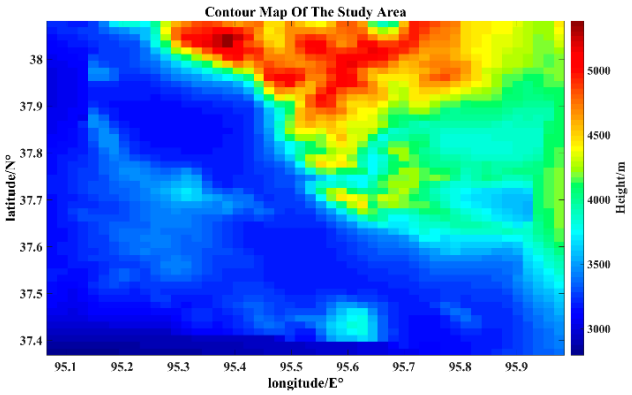

Figure 1. Study area plane contour diagram.

Table 1. IGBP land cover classification table.

Corresponding Numbers	Types
1	Evergreen Needleleaf Forest
2	Evergreen Broadleaf Forest
3	Deciduous Needleleaf Forest
4	Deciduous Broadleaf Forest
5	Mixed Forest
6	Closed Shrubland
7	Open Shrubland
8	Woody Savanna
9	Savanna

Table 1. *Cont.*

Corresponding Numbers	Types
10	Grassland
11	Permanent Wetland
12	Cropland
13	Urban and Built-Up Area
14	Mosaic of Cropland and Natural Vegetation
15	Snow and Ice
16	Barren Land (Desert)

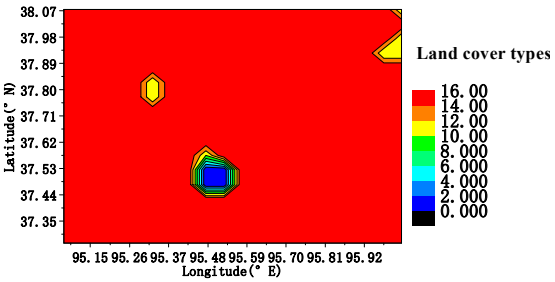

Figure 2. Distribution of species covered by the surface cover in the study area.

2.2. Scene Layout for Mid-Wave Infrared Hyperspectral Imaging Experiment

The experiment was conducted from the 4th of August to the 7th of August 2020. The measurement targets were distributed in different areas, so the experiment was conducted in two different scenes, as shown in Figure 3a,b.

(**a**) (**b**) (**c**)

Figure 3. Actual shooting of experimental measurement site; target site 1 (**a**), target site 2 (**b**), equipment site (**c**).

Scene 1:

- Geographic coordinates: (95.35°E, 37.85°N)
- Altitude: 3748 m
- Main measurement target: Grassland
- Distance from the measurement point to the surface: 116.7 m (slant distance)
- Measurement azimuth: Southwest (209°)
- Measurement elevation angle: 11°
- Measurement height difference: Approximately 15 m

Scene 2:

- Geographic coordinates: (95.33°E, 37.88°N)
- Altitude: 3762 m
- Main measurement target: Gobi Desert
- Distance from the measurement point to the desert: 158.1 m (slant distance)
- Measurement azimuth: Northwest (298°)
- Measurement elevation angle: 11°
- Measurement height difference: Approximately 16 m

The setup of the measurement equipment site is illustrated in Figure 3c, and the schematic diagrams of the measured scenes are shown in Figure 4a,b.

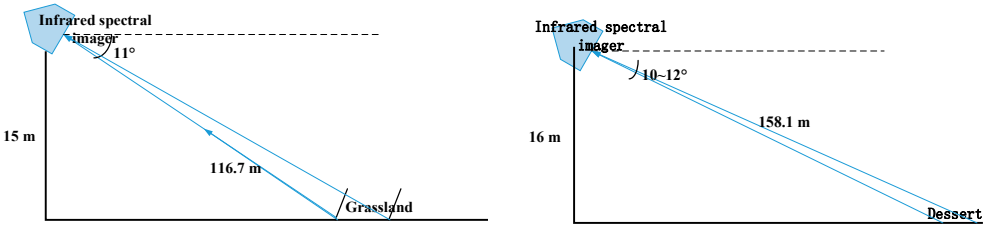

(**a**) (**b**)

Figure 4. Schematic diagram of a typical land surface survey scene; grassland (**a**), Gobi Desert (**b**).

2.3. Main Measured Instrument Specifications

The main measurement instruments used in this experiment are as follows: the Hyper-Cam (extended mid-wave hyperspectral imaging instrument), as shown in Figure 5a; the SSN-61 thermocouple temperature acquisition instrument, as shown in Figure 5b; and the IBS-F60 combined weather station [30], as shown in Figure 5c.

(**a**) (**b**) (**c**)

Figure 5. The main instruments used in the experiment: Hyper-Cam extended medium-wave spectroscopy imager (**a**); SSN-61 thermocouple temperature acquisition instrument (**b**); IBS-F60 combined weather station (**c**).

The main instrument parameters used in this experiment are shown in Tables 2–4.

Table 2. Main technical parameters of the Hyper-Cam (extended medium-wave spectroscopy imager).

Parameters	Technical Indicators
Spectral Range	1.5–5 μm
Spectral Resolution	0.25–150 cm^{-1}
Spatial Resolution	320 × 256 pix
Detector	MCT Stirling cooled
Instantaneous Field of View	0.35 mrad
Equivalent Noise	<7 nw/(cm^2·sr·μm)
Measurement Accuracy	±0.95 K

Table 3. Technical parameters of the SSN-61 thermocouple temperature acquisition instrument.

Parameters	Technical Indicators
Measurement Range	−180~1250 °C
Measurement Accuracy	±0.5%
Resolution	0.1 °C
Number of Recordable Datasets	31,998
Operating Temperature	−35~80 °C
Battery Operating Temperature	−35~80 °C

Table 4. Technical parameters of the IBS-F60 combined weather station.

Parameters	Technical Indicators
Wind Speed Measurement Range	0~70 m/s
Wind Speed Measurement Accuracy	±0.3 m/s
Wind Direction Measurement Range	0~360°
Wind Direction Measurement Accuracy	±0.1°
Air Pressure Measurement Range	10~1100 hPa
Air Pressure Measurement Accuracy	±0.3 hPa
Air Temperature Measurement Range	−50~60 °C
Air Temperature Measurement Accuracy	±0.3 °C
Humidity Measurement Range	0~100% RH
Humidity Measurement Accuracy	±0.3% RH

2.4. Experiment Measurement Plan

In addition to the hyperspectral imaging measurement in the mid-wave infrared range, several auxiliary parameters were measured, including meteorological parameters and surface temperature of the targets.

(1) Meteorological Parameter Measurement:

The IBS-F60 combined weather station was used to measure meteorological parameters such as temperature, humidity, atmospheric pressure, and visibility in the measured field.

(2) Measurement of Target Surface Temperature:

The surface temperature of the targets is essential for the retrieval and validation of satellite remote sensing parameters such as land surface temperature (LST) and land surface emissivity (LSE). The surface temperatures of the grassland and Gobi Desert were measured using a thermocouple temperature acquisition instrument.

(3) Ground Target Mid-Wave Infrared Hyperspectral Imaging Measurement

Measurement was conducted using the Hyper-Cam mid-wave hyperspectral imaging instrument developed by Telops. After calibrating the measuring equipment, the ground targets were subjected to hyperspectral imaging measures in the mid-wave infrared range. A dataset was collected every half hour.

2.5. Verification of Spectral LSE and LST Inversion

2.5.1. Theoretical Framework for Spectral LSE and LST Inversion

The calculation scheme used for the verification of temperature and emissivity inversion for different land surface types is shown in Figure 6.

The overall calculation process, as shown in Figure 6, is as follows: First, the measurement data undergoes noise removal using a Gaussian filter, and the atmospheric transmission characteristics parameters are calculated using Modtran4.0 to perform atmospheric correction on the surface medium-wave high-spectral imaging data. Then, Modtran4.0 is utilized to calculate the solar irradiance and atmospheric background radiation. The surface bidirectional reflectance distribution function (BRDF) model is applied to mitigate the scattering effects of sunlight and atmospheric background radiation on the surface.

Considering the rectangular area of the experimental observations, it can be approximated as a point in relation to the 5.56 km spatial resolution of MODIS imagery. In order to address the spatial resolution disparity between ground and satellite scales, this experiment selects sampling sites with high homogeneity and good spatial representativeness. The point-to-area upscaling method is employed [31], where the values of ground sampling points are directly averaged in order to match the spatial resolution of the ground observation data.

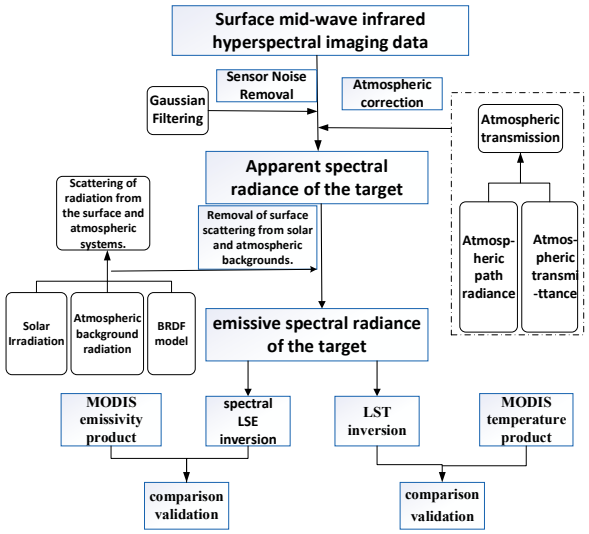

Figure 6. Calculation scheme for the inversion verification of different types of surface temperature and emissivity.

Subsequently, a comparison and a validation are conducted by comparing the redistributed satellite data with the ground observation data. Finally, the processed data is used for spectral land surface emissivity (LSE) and land surface temperature (LST) inversion, and the results are compared and validated using MODIS products.

(1) Noise Estimation and Removal

(a) Sensor Noise Estimation

The noise level performance was evaluated in the laboratory using the noise equivalent spectral radiance (NESR) metric to assess the noise level of the Hyper-Cam MW sensor. Based on the imaging principle of the Hyper-Cam MW sensor with a specific optical system, the NESR is related to the spectral resolution and integration time of the Hyper-Cam MW sensor. In the noise level estimation, NESR is calculated as the pixel-wise standard deviation of the radiance from multiple consecutive data cubes of the same target [24]. The noise calculation results are shown in Figure 7.

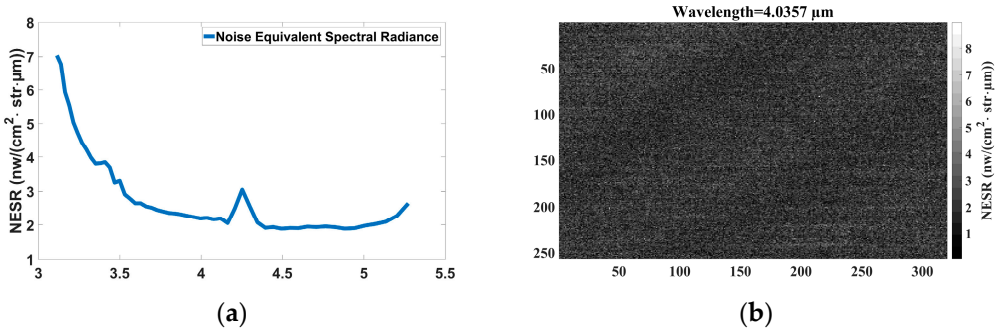

Figure 7. Noise calculation results: (**a**) average spectral NESR; (**b**) visualization of 4.0357 μm noise image.

Figure 7 showed that after performing the average spectral NESR calculation, within the range of 3 to 3.5 μm, the NESR increases with increasing wavelength, and there is a relatively high level in this range. Near 4.2 μm, there is a peak, which is caused by a significant increase in path radiance due to the presence of a carbon dioxide atmospheric absorption band in the vicinity of that wavelength.

(b) Sensor Noise Removal Based on Gaussian Filtering

Both the entire mid-wave infrared hyperspectral image and the noise within random windows approximate a Gaussian distribution. Therefore, Gaussian convolution is applied

as a spatial denoising method in order to improve the noise quality in each spectral band. This approach takes into account that the noise type in small windows also approximates a Gaussian distribution. It calculates a weighted template using the Gaussian kernel model and then convolves the weighted template with the entire moving window of the hyperspectral image. The window size of the Gaussian template is 3 × 3 pixels. Gaussian filtering for spatial denoising can effectively remove noise from the experimental image while preserving the atmospheric features present in the captured data [24]. The denoising results are shown in Figures 8 and 9.

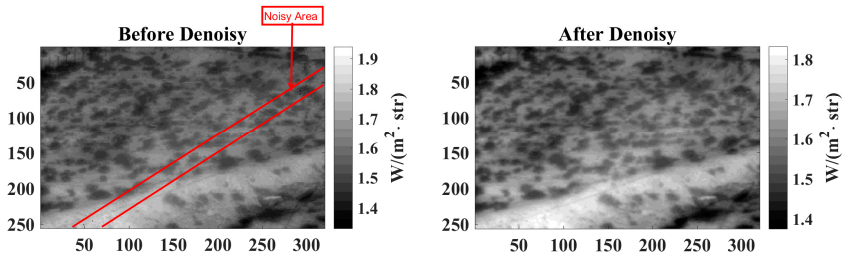

Figure 8. Comparison before and after denoising of the integrated image in the range of 3–5 μm.

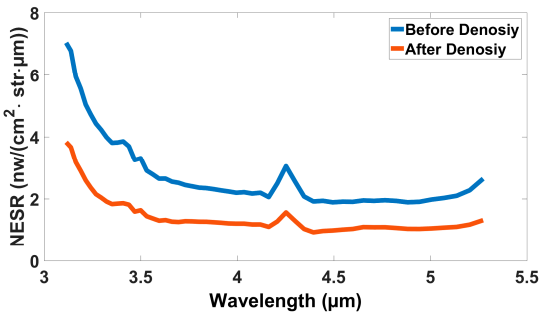

Figure 9. Comparison of NESR before and after denoising.

Figures 8 and 9 showed that after applying Gaussian spatial convolution filtering, the regions with correlated noise in the original measured image are significantly removed, and the NESR shows a noticeable decrease. This process enhances the image quality of the hyperspectral data, resulting in improved clarity and reduced noise interference.

(2) Atmospheric correction:

During the experiment, the radiation detected by the sensor includes three components: atmospheric path radiance, scattering of the target's own radiation by sunlight and atmospheric background radiation, and the target's own thermal radiation. The spectral radiance received by the detector is expressed in Equation (1).

$$L(\lambda) = \tau_{atm}(\lambda) \cdot [L_{self}(\lambda) + L_{reflect\_bg}(\lambda)] + L_{path}(\lambda) \quad (1)$$

In order to remove the influence of atmospheric transmission, atmospheric correction is applied to the measured data so as to eliminate the effects of atmospheric path radiance and transmission attenuation, thereby obtaining the apparent radiance of the target. The processing method is shown in Equation (2).

$$L'(\lambda) = L_{self}(\lambda, T, \varepsilon_\lambda) + L_{reflect\_bg}(\lambda) = \frac{L(\lambda) - L_{path}(\lambda)}{\tau_{atm}(\lambda)} \quad (2)$$

According to Equation (2), the atmospherically corrected data include the target's thermal radiation and the scattering of the target's radiation by sunlight and atmospheric background radiation. In order to accurately invert the emissivity, it is necessary to remove the scattering of the target by sunlight and atmospheric background radiation, thereby

obtaining the target's own thermal radiation. The calculation expression for the target's self-radiation characteristics is shown in Equation (3).

$$L_{self}(T,\varepsilon,\lambda) = \frac{L(\lambda)-L_{\text{path}}(\lambda)}{\tau} - [f_{\text{r}}(I_r,\phi_r;I_s,\phi_{\text{s}},\lambda)\cdot E_{\text{sun}}(\lambda)\cdot\cos I_r + \rho(2\pi;I_s,\phi_s,\lambda)L_{\text{sky}}(\lambda)] \quad (3)$$

In Equation (3), $L(\lambda)$ represents the measured surface spectral radiance, I_r represents the solar zenith angle under actual terrain conditions, $f_{\text{r}}(I_r,\phi_r;I_{\text{s}},\phi_{\text{s}},\lambda)$ represents the surface anisotropic reflectance, $\rho(2\pi;I_s,\phi_s,\lambda)$ represents the surface hemispherical-directional reflectance, E_{sun} represents the solar irradiance, L_{sky} represents the sky background radiance, $\tau(\lambda)$ represents the transmittance of the detection path, and $L_{\text{path}}(\lambda)$ represents the radiance of the detection path.

All atmospheric transmission parameters, such as atmospheric path radiance, atmospheric transmittance, solar radiation irradiance, and sky background radiance, are calculated using Modtran4.0. The surface anisotropic reflectance and surface hemispherical–directional reflectance can be obtained through inversion using MOD43C1 products.

(3) Spectral Land Surface Emissivity (LSE) Inversion:

The spectral LSE is inverted using the Planck blackbody radiation formula. The inversion equation for spectral LSE is shown in Equation (4).

$$\varepsilon(T,\ \lambda) = \frac{[\exp(c_2/(\lambda T))-1]\cdot\pi\cdot\lambda^5\cdot L_{self}(T,\lambda)}{c_1} \quad (4)$$

$$c_1 = 2\pi hc^2 = 3.7415\times10^8\ \text{W}\cdot\mu\text{m}^4\cdot\text{m}^{-2}; c_2 = ch/k = 1.43879\times10^4\ \mu\text{m}\cdot\text{k};$$

In Equation (4), $L_{self}(T,\lambda)$ represent the thermal radiation spectrum of the surface background, T represent the temperature (in Kelvin), and λ represent the wavelength (in μm), respectively.

(4) Land Surface Temperature (LST) Inversion:

The equation for LST inversion is shown in Equation (5).

$$L_{self}(T) = \int_{3\mu\text{m}}^{5\mu\text{m}} \varepsilon\cdot\frac{c_1}{\lambda^5}\cdot\frac{1}{\exp^{\frac{c_2}{\lambda T}}-1}d\lambda \quad (5)$$

In Equation (5), ε represent the surface emissivity, $L_{self}(T,\lambda)$ represent the thermal radiation spectrum of the surface background (in $\text{W}/(\text{m}^2\cdot\text{sr})$), T represent the temperature (in Kelvin), and λ represent the wavelength (in μm), respectively.

2.5.2. Acquisition of Surface Background BRDF

In order to remove the scattering component of the target by sunlight and atmospheric background radiation, the anisotropic scattering of the surface needs to be considered. A linear kernel-driven BRDF model is used to solve this problem. For the two natural land surface types (grassland and desert), BRDF parameter data of the surface can be obtained from the MCD43C1 product. The MCD43C1 product provides global surface reflectance, bidirectional reflectance distribution function (BRDF) parameters. These parameters are derived from data collected by the Terra and Aqua satellites of the MODIS (moderate resolution imaging spectroradiometer) system. The spatial resolution of each pixel is 0.05 degrees. The MCD43C1 data product is generated through processing and analysis of the radiance measurements in different spectral bands. This product provides the linear weighting coefficients of the RossThick-LiSpare-Reciprocal BRDF model for bands 3 to 5 μm [32]. The surface reflectance is a linear combination of isotropic scattering, volumetric

scattering, and geometric optical surface scattering [33,34], as shown in Equation (6). Using this equation, the bidirectional reflectance at any incident and viewing angles can be obtained.

$$\rho(\theta_r, \theta_s, \varphi) = f_{iso}K_{iso} + f_{vol}K_{vol}(\theta_r, \theta_s, \varphi) + f_{geo}K_{geo}(\theta_r, \theta_s, \varphi) \quad (6)$$

In Equation (6), θ_r represent the incident zenith angle, θ_s represent the viewing zenith angle, and φ represent the relative azimuth angle between the viewing direction and the radiation incident direction, respectively. Additionally, f_{iso},f_{vol},f_{geo} represent the proportion coefficients of isotropic scattering kernel, volumetric scattering kernel, and surface scattering kernel in the linear combination, which can be obtained from the MCD43C1 product.

In MODIS products, the isotropic scattering kernel is defined as $K_{iso} = 1$. For the volume scattering kernel, the volumetric scattering kernel model proposed by Roujean is used [33]. This model mainly describes densely vegetated layers with similar distribution of leaves, implying that their reflectance can be considered somewhat equivalent. The expression for the volume scattering kernel is as follows [35]:

$$K_{vol} = \frac{(\frac{\pi}{2} - \xi)\cos\xi + \sin\xi}{\cos\theta_r + \cos\theta_s} - \frac{\pi}{4} \quad (7)$$

ξ represents the phase angle, which is related to the solar zenith angle, the viewing zenith angle, and their relative azimuth angle:

$$\cos\xi = \cos\theta_i \cos\theta_v + \sin\theta_i \sin\theta_v \cos\varphi \quad (8)$$

For the geometric optical surface scattering kernel K_{geo}, considering the mutual occlusion between vegetation canopies, the modified LiSparse [34] model proposed by Lucht is used. The specific expression is as follows:

$$K_{geo} = H(\theta'_r, \theta'_s, \varphi) - \sec\theta'_r - \sec\theta'_s + \frac{1}{2}(1 + \cos\xi')\sec\theta'_r \sec\theta'_s \quad (9)$$

$H(\theta'_r, \theta'_s, \varphi)$ represents the overlap region between the observation and the solar shadow, and the specific formula is:

$$H(\theta'_r, \theta'_s, \varphi) = \frac{1}{\pi}(t - \sin t \cos t)(\sec\theta'_r + \sec\theta'_s) \quad (10)$$

The expressions for other parameters are as follows:

$$\begin{aligned} \theta'_r &= \arctan(\tfrac{b}{r}\tan\theta_r) \\ \theta'_s &= \arctan(\tfrac{b}{r}\tan\theta_s) \end{aligned} \quad (11)$$

$$\cos t = \frac{h}{b} \cdot \frac{\sqrt{D^2 + (\tan\theta'_r \tan\theta'_s \sin\varphi)}}{\sec\theta'_r + \sec\theta'_s} \quad (12)$$

$$D = \sqrt{\tan^2\theta'_r + \tan^2\theta'_s - 2\tan\theta'_r \tan\theta'_s \cos\varphi} \quad (13)$$

$$\cos\xi' = \cos\theta'_r \cos\theta'_s + \sin\theta'_r \sin\theta'_s \cos\varphi \quad (14)$$

In MODIS products, the parameter $h/b = 2, b/r = 1$ is defined as a dimensionless parameter representing the relative height and shape of the canopy top. Combining Equations (6) to (14), the linear weighting coefficients of the BRDF for different land surface backgrounds in 2020, obtained from the MCD43C1 product, are shown in Figure 10.

Figure 10 showed that the isotropic scattering kernel weight (f_{iso}) contributes the most to both land surface types, and it exhibits significant fluctuations throughout the four seasons. This can be attributed to the relatively uniform biological and physical structure of the land surface vegetation, allowing the weight coefficient to effectively capture the

temporal variations of the actual land surface biophysical properties. The contribution of the volume scattering kernel (f_{vol}) shows slightly smaller fluctuations compared to the isotropic scattering contribution (f_{iso}), which can be attributed to the inherent differences in biological properties and structural characteristics of barren land and grassland. The Fvol values remain relatively low throughout the year. The contribution of the geometric scattering kernel (f_{geo}) is the lowest for both land surface types, representing the correction for mutual occlusion. It is noteworthy that the f_{geo} values for grassland and barren land tend to approach zero, validating this conclusion.

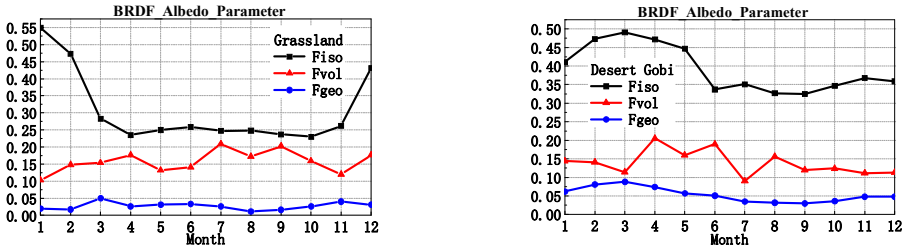

(**a**) (**b**)

Figure 10. Time series changes of two natural linear combined land surface weight coefficients in 2020; (**a**) grassland, (**b**) Gobi Desert.

By utilizing the geometric positions of the sun and the detector, as shown in Table 5, and combining them with Equation (6), the anisotropic reflectance of the land surface can be calculated. The calculated BRDF values for the grassland and the Gobi Desert are 0.043 and 0.075, respectively.

Table 5. Detailed data of geometric position in experimental environment.

Ground Cover	Grassland	Desert
Time	6th August, 15:00	7th August, 15:00
Solar geometry	Solar zenith angle: 45.07°, Solar azimuth angle: 106.01°	
Detector geometry	Detector zenith angle: 79°	Detector azimuth angle: 78°
Azimuth angle	188°	326°
Location	95.35°E; 37.85°N	95.33°E; 37.88°N
Size of the measure area	131.4 m^2	246.4 m^2

2.5.3. Typical Surface Emissivity and MODIS Reflectance Data Product Retrieval

(1) Surface Emissivity Retrieval

Emissivity data for the desert and grassland in the northwest plateau region of China in 2020 were obtained from the MOD11 product. These data are used for comparative validation of the spectrally emissivity inversion obtained from the mid-wave hyperspectral imaging measurements. The MODIS product provides three narrow-band reflectance data in the mid-wave infrared region, namely Band20 (3.66~3.840 μm), Band22 (3.929~3.989 μm), and Band23 (4.010~4.080 μm). The temporal variation of emissivity for grassland and desert in these three bands in 2020 is shown in Figure 11.

According to the analysis from Figure 11, the emissivity of grassland surface varies between 0.934 and 0.985 throughout the year, showing consistency across the three mid-infrared bands. In March, it reaches the lowest value of 0.934, while it reaches the maximum value in July. From July to December, the emissivity values gradually decrease. In August, he mid-infrared emissivity values for grassland are 0.968, 0.96, and 0.956. On the other hand, the emissivity of barren land surface fluctuates between 0.806 and 0.970, showing larger variations throughout the year. In September, the mid-infrared emissivity values for barren land are 0.9545, 0.93, and 0.886.

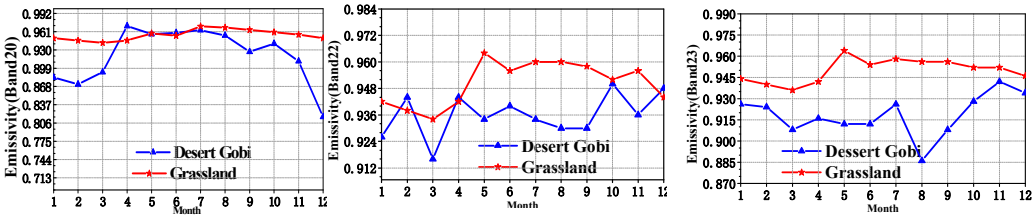

(a) (b) (c)

Figure 11. The variations of typical surface emissivity over time series in the mid-wave infrared band. (**a**) Band20; (**b**) Band22: (**c**) Band23.

(2) Retrieval of Hemispherical-Directional Reflectance for Natural Surfaces

According to the directional Kirchhoff law [36], for opaque objects, the relationship between the directional emissivity and the hemispherical–directional emissivity can be expressed as:

$$\varepsilon(\lambda,\theta,\phi) = 1 - r(\lambda,\theta,\phi) = 1 - \int_0^{2\pi}\int_0^{\frac{\pi}{2}} f(\theta_r,\phi_r,\theta_s,\phi_s,\lambda)\cos\theta_r \sin\theta_r d\theta_r d\phi_r \quad (15)$$

By combining Equation (6), the mid-wave infrared hemispherical-directional emissivity can be obtained as:

$$\varepsilon(\theta) = 1 - f_{iso}K_{iso} - f_{vol}IK_{vol}(\theta) - f_{geo}IK_{geo}(\theta) \quad (16)$$

$$IK_a(\theta) = \frac{1}{\pi}\int_0^{2\pi}\int_0^{\frac{\pi}{2}} f_a(\theta_r,\theta_s,\varphi)\sin\theta_r\cos\theta_r d\theta_r d\phi, a = vol/geo \quad (17)$$

From Equation (8), it can be observed that, based on the weights $(f_{iso}, f_{vol}, f_{geo})$, the hemispherical-directional emissivity of the surface can be obtained at different angles. The variation trends of the hemispherical–directional emissivity for grassland and desert in the infrared wavelength range during different seasons are shown in Figure 12, considering the weighting coefficients provided in Figure 10.

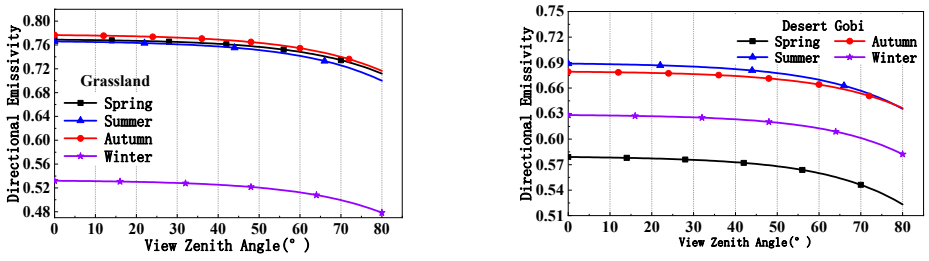

(**a**) (**b**)

Figure 12. Hemispherical–directional emissivity in different seasons in typical surface infrared bands. (**a**) Grassland; (**b**) Gobi Desert.

Figure 12 showed that the mid-wave hemispherical emissivity of grassland and barren land surfaces shows a similar trend. It remains relatively stable for observation zenith angles between 0° and 40° and starts to decrease from 40° to 80°. From a temporal perspective, there is a distinct difference in the grassland environment during winter compared to other seasons. The hemispherical emissivity of grassland is the lowest in winter, ranging from 0.48 to 0.53, while in the other three seasons, it ranges from 0.72 to 0.78. On the other hand, the hemispherical emissivity of barren land fluctuates between 0.5 and 0.7, with the highest values being observed in summer, followed by autumn, winter, and spring. This phenomenon is mainly related to vegetation characteristics and properties.

3. Research Results and Discussion

3.1. Calculation Results of Atmospheric Transmission Parameters

During the high-spectral imaging measurement of the target, simultaneous measurements of the environmental parameters in the measurement area were conducted using the IBS-F60 thermocouple temperature acquisition instrument and the SSN-61 comprehensive meteorological station, and the results are shown in Table 6. Based on these environmental parameters, atmospheric profile data corresponding to the study area, time, and location were obtained from the European Centre for Medium-Range Weather Forecasts (ECMWF), as shown in Figure 13, The original data are divided into four seasons: spring, summer, autumn, and winter. The mean values of temperature, humidity, and pressure are calculated for each season over a period of 36 months. Additionally, the original data are interpolated based on different altitude ranges. Specifically, interpolation is performed every 0.5 km from 0 km to 10 km in height, every 1 km from 11 km to 20 km, every 3 km from 21 km to 30 km, and specific data points are selected at 33 km, 35 km, and 40 km for the range of 31 km to 40 km. In total, there are 38 layers, with the highest altitude reaching approximately 40 km. Finally, using the MODTRAN software, custom inputs for temperature, humidity, pressure, and the environmental parameters from Table 4 were provided in order to calculate the atmospheric transmission parameters. The input conditions for Modtran 4.0 calculations were as follows: a custom study area model, 7 August 2020 (day 220), clear sky conditions without clouds or rain, an observation height of 3.7 km, solar zenith angle of 45.07°, and solar azimuth angle of 106.01°. The calculated results of the atmospheric transmission characteristics from the target to the sensor are shown in Figure 14.

Table 6. Environmental parameters of the experimental site.

Measurement Information	Environment Values
Location	95.35°E; 37.85°N
Measure time	7 August 2020, 15:00 local time
Humidity	49.6%
Weather cinditions	Clear sky, no clouds
Height difference between target and measured point	16 m
Straight-line distance between target and measured point	116.7 m
Experimental measured temperature of grassland	292.6 K
Experimental measured temperature of desert	325.93 K

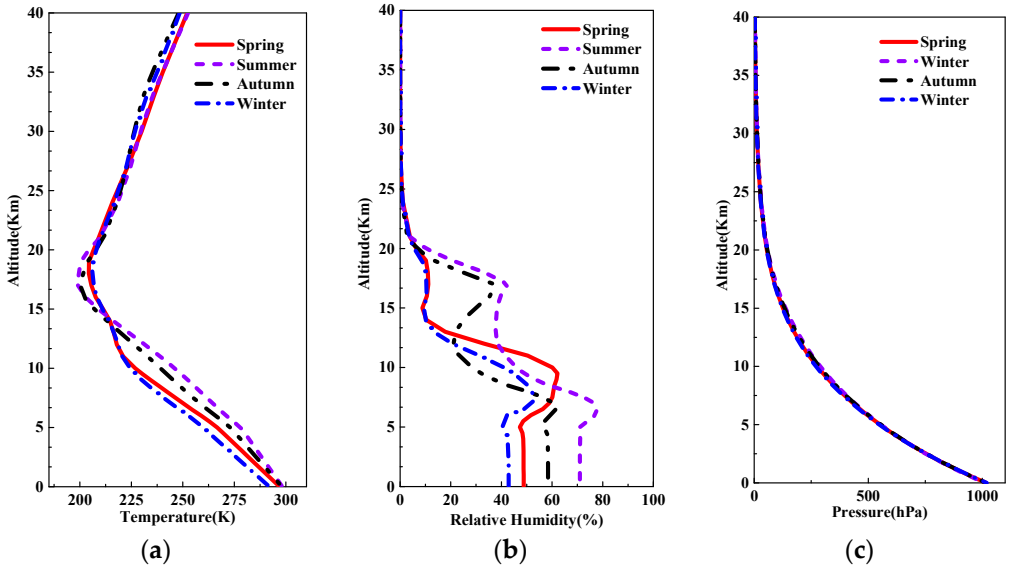

Figure 13. Atmospheric profile distribution curves in different seasons in the study area. (**a**) Temperature; (**b**) humidity; (**c**) pressure.

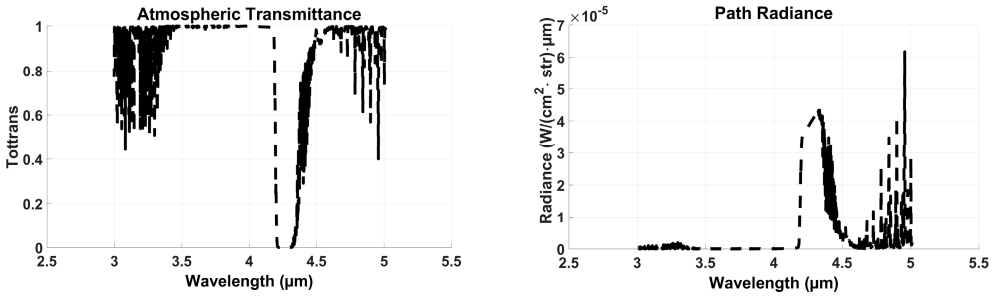

Figure 14. Atmospheric transmission characteristics on the target-to-sensor path;spectral transmittance (**a**) and path radiation (**b**).

Figure 13 showed that in the altitude range of 0 to 18 km, the temperature decreases with increasing altitude, which is due to the presence of the troposphere. Within this range, as the altitude increases, the atmospheric pressure and density gradually decrease, and the vertical movement of air also leads to temperature decrease. However, in the altitude range above 18 km, as the altitude further increases, the temperature begins to rise again, which is due to the presence of the stratosphere. The stratosphere is the upper part of the atmosphere, where the temperature gradually increases with altitude. This is because the stratosphere contains an ozone layer, and ozone molecules absorb ultraviolet radiation from the sun and convert it into heat energy, resulting in an increase in stratospheric temperature. Regarding humidity, it remains relatively stable in the altitude range of 0 to 5 km, with higher values observed in summer compared to autumn, spring, and winter. Above 5 km, there is a trend of initially increasing and then decreasing humidity, with almost negligible humidity levels beyond 25 km. On the other hand, the atmospheric pressure shows minimal variations among the four seasons, decreasing with increasing altitude.

Figure 14 showed that the atmospheric transmittance is almost zero around 4.3 μm, and the atmospheric path radiance continues to increase in this spectral band. As a result, the detector cannot accurately measure the true spectral radiance of the surface in this band. The calculated results of sky background radiance and solar irradiance are shown in Figure 15. It can be seen from Figure 15 that the solar irradiance received by the target surface decreases with decreasing wavelength. In the range of 4.2 to 4.5 μm, the solar irradiance is almost zero, while the sky background radiance exhibits a peak in this band. Therefore, the radiance received by the detector in this band is mostly generated by the atmosphere.

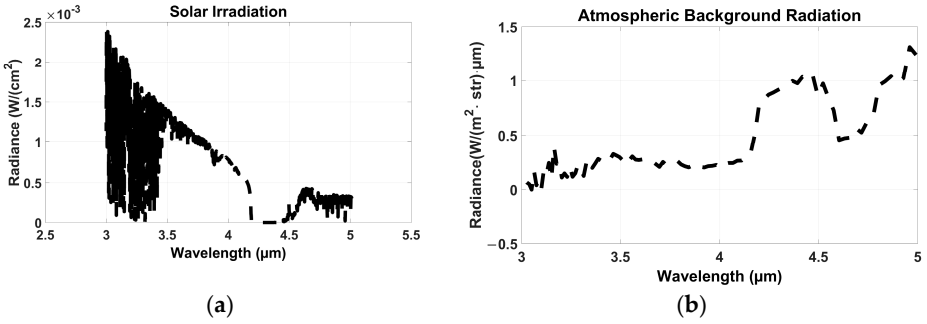

Figure 15. Sky background radiation and solar radiation irradiance. (**a**) Solar irradiance; (**b**) sky background radiation.

3.2. Inversion of Mid-Wave Infrared Spectral Emissivity and Validation with MOD11C1 Emissivity Product

After eliminating the influence of scattering from solar and sky background radiance, the spectral emissivity was calculated using the experimental temperature values and Equation (4). In order to validate the results, the obtained spectral emissivity was compared

with the spectral reflectance of Band20, Band21, and Band22 channels in the MOD11C1 emissivity product. However, considering that the experimental observation area was a rectangular region of 13 m × 0 m (14 m × 17 m), which can be considered as a point relative to the spatial resolution of 5.56 km in MODIS imagery, the spatial resolution difference between ground and satellite scales needed to be addressed. In this experiment, the sampled ground points demonstrated a high level of uniformity, and the sampling sites had good spatial representativeness. Therefore, a point-to-area upscaling conversion method was used, where the ground sample point values were directly averaged arithmetically to match the spatial resolution of the ground observation data. Finally, a comparison and validation were conducted between the redistributed satellite data and the ground observation data. Spectral emissivity based on hyperspectral imaging data inversion and the emissivity values in the three discrete channels of MOD11C1 in the mid-wave infrared spectrum (the center wavelengths of narrow spectral bands are used to represent the wavelength) are shown in Figure 16.

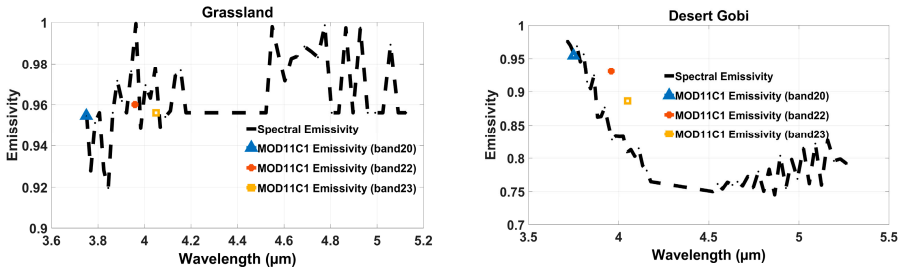

Figure 16. Spectral emissivity based on hyperspectral imaging data inversion and MOD11C1 emissivity. (**a**) Grassland; (**b**) Gobi Desert.

Figure 16 showed that, in the experimental measurements of the mid-wave infrared spectrum, the emissivity of the grassland remains around 0.95, symmetrically distributed on both sides of the atmospheric absorption band. On the other hand, the emissivity of the Gobi Desert shows a decreasing trend with increasing wavelength. Since MOD11C1 provides emissivity values in three narrow bands, for the purpose of visualization, the wavelengths of the three channels in MOD11C1 were chosen as the medians of their respective narrow bands. Therefore, there is a spectral scale issue in the validation of MOD11C1 emissivity products, and the inversion of surface emissivity needs to be obtained in the narrow bands consistent with the three satellite channels. Table 7 shows the absolute and relative errors between the emissivity values of the three channels provided by MOD11C1 and the inversion data. It can be seen from the table that, compared to the Gobi Desert, the grassland has larger errors in Band20 and Band23. In the emissivity data of the grassland from MOD11C1, the emissivity in Band20 is overestimated, while in the other two bands, it is underestimated. Conversely, for the Gobi Desert, the emissivity in Band20 is underestimated, while in the other bands, it is overestimated. However, overall, the absolute errors of the three narrow-band emissivity values provided by MOD11C1 in the 3–5 micron wavelength range are all within 5%, indicating that MOD11C1 still maintains a high level of accuracy in its emissivity products in the mid-wave infrared spectrum.

Table 7. MOD11C1 mid-wave infrared emissivity product and emissivity comparison error table based on hyperspectral imaging data inversion.

Wavelength Range	LandSurface Type	Absolute Error	Relative Error
Band20 (3.66~3.840 μm)	Grassland	0.0376	3.9%
Band22 (3.929~3.989 μm)	Grassland	0.0191	2.1%
Band23 (4.010~4.080 μm)	Grassland	0.0429	4.8%
Band20 (3.66~3.840 μm)	Desert Gobi	0.0057	0.4%
Band22 (3.929~3.989 μm)	Desert Gobi	0.0458	4.9%
Band23 (4.010~4.080 μm)	Desert Gobi	0.0412	3.9%

3.3. Comparison and Validation of MOD11L2 Temperature Product with Temperature Field Inversion Based on Mid-Wave Infrared Hyperspectral Measured Data

The temperature fields of the grassland and Gobi desert land surfaces were inverted using Equation (5) based on the mid-wave infrared hyperspectral imaging measurements acquired at 15:00 in the afternoon. The inversion results are shown in Figure 17. In order to match the spatial resolution of the ground observation data and maintain consistency with MODIS data, a point-to-area upscaling conversion method was employed, where the values of ground sample points were arithmetically averaged. The inverted temperature fields were then compared and validated against the extracted MOD11L2 remote sensing temperature data. The comparison and validation results are presented in Table 8.

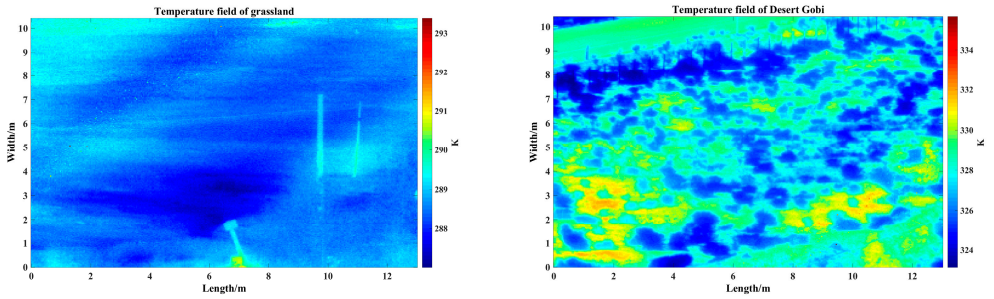

(**a**) (**b**)

Figure 17. Two natural surface temperature field inversion diagrams. (**a**) Grassland; (**b**) Gobi Desert.

Table 8. Comparison of verification data and errors.

Land Surface Type	Grassland	Gobi Desert
RemoteSensingTemperature (K)	293.7	323.9
Inverted Temperature (K)	289.5	321.6
Absolute Error (K)	±4.2	±2.3
Relative Error	1.4%	0.7%

According to Table 8, it can be seen that both the remote sensing temperature and the inverted temperature of the desert and Gobi are higher than that of the grassland at the same time, which is due to the difference in their specific heat capacities. Furthermore, the remote sensing temperatures obtained from MOD11L2 for both the grassland and the desert and Gobi are underestimated. The absolute errors of the MOD11L2 grassland temperature product and the desert and Gobi temperature product are ±4.2 K and ±2.3 K, respectively. The relative error of the temperature product in the desert and Gobi is smaller than that in the grassland, with a relative error within 2%. Through the comparative verification, it can be concluded that both datasets are effective means for studying the infrared radiation characteristics of typical land cover types.

4. Conclusions

This study is based on a middle-wave infrared hyperspectral imaging measured dataset of typical ground backgrounds in the northwest region of China, covering the period from the 4th of August to the 7th of August 2020. The main focus is to validate the accuracy of the MOD11C1 and MOD11L2 products in terms of land surface emissivity (LSE) and land surface temperature (LST). After evaluating and removing noise from the measured dataset, performing atmospheric correction, and eliminating the scattering components from solar and sky background radiation, the spectral emissivity and temperature field of the measured area were inverted. The inverted data were then compared and validated against the MODIS land surface temperature (LST) and emissivity (LSE) products. The validation results demonstrate that the absolute errors of the three middle-wave infrared narrow bands (Band20: 3.66–3.840 μm, Band22: 3.929–3.989 μm, Band23: 4.010–4.080 μm) for grassland emissivity in the MOD11C1 product are 0.0376, 0.0191, and

0.0429, respectively. The corresponding relative errors are 3.9%, 2.1%, and 4.8%, respectively. For the three middle-wave infrared narrow bands (Band20: 3.66–3.840 μm, Band22: 3.929–3.989 μm, Band23: 4.010–4.080 μm) related to desert emissivity in the MOD11C1 product, the absolute errors are 0.0057, 0.0458, and 0.0412, respectively, with relative errors of 0.4%, 4.9%, and 3.9%, respectively. The relative errors for each channel are all within 5%. In the MOD11L2 temperature product, the absolute errors of the remotely sensed temperature for the desert and grassland are ±2.3 K and ±4.1 K, respectively, with relative errors of 0.7% and 1.4%. The relative errors of the temperature product are all within 2%.

The climate variation in the northwest region of China is profound. Utilizing of MODIS data can significantly assist government agencies and research institutions in devising more effective desertification control measures and climate adaptation strategies. Simultaneously, the acquisition of land surface temperature and land surface emissivity data holds immense value for forestry and agricultural management as it aids in monitoring the growth status of farmland and forests. Additionally, it enables timely monitoring and early warning during natural disasters such as droughts and floods. Hence, the evaluation of MODIS LST and LSE products is of utmost importance. In this study, a precise assessment of MODIS temperature and emissivity products was conducted, providing users with data accuracy while further contributing to advancements in LST detection methodologies. Evaluating the accuracy of the latest MODIS LST and LSE products will drive their expanded utilization across diverse application domains.

Author Contributions: Conceptualization, Y.J. and Y.C. (Yunhua Cao); data curation, Y.J. and Y.C. (Yisen Cao); methodology, Z.W.; validation, Y.J. and Y.C. (Yisen Cao); writing—original draft, Y.J.; writing—review and editing, Y.C. (Yunhua Cao). All authors have read and agreed to the published version of the manuscript.

Funding: This research is supported by the 111 Project (Grant No. B17035) and the National Natural Science Foundation of China (61875156).

Data Availability Statement: Not applicable.

Acknowledgments: The authors are grateful to the anonymous reviewers for their critical review, insightful comments, and valuable suggestions.

Conflicts of Interest: The authors declare no conflict of interest.

References

1. Tong, K.; Su, F.; Yang, D.; Hao, Z. Evaluation ofsatellite precipitation retrievals and their potential utilities in hydrologic modeling over the Tibetan Plateau. *J. Hydrol.* **2014**, *519*, 423–437. [CrossRef]
2. Blum, M.; Lensky, I.M.; Nestel, D.J.A.; Meteorology, F. Estimation of olive grove canopy temperature from MODIS thermal imagery is more accurate than interpolation from meteorological stations. *Agric. For. Meteorol.* **2013**, *176*, 90–93. [CrossRef]
3. Sharifnezhadazizi, Z.; Norouzi, H.; Prakash, S.; Beale, C.; Khanbilvardi, R. A Global Analysis of Land Surface Temperature Diurnal Cycle Using MODIS Observations. *J. Appl. Meteorol. Climatol.* **2019**, *58*, 1279–1291. [CrossRef]
4. Mohammad, S.; Wolfgang, R.; Peyman, Z.R.J.R.S. Analysis of MODIS LST Compared with WRF Model and in situ Data over the Waimakariri River Basin, Canterbury, New Zealand. *Remote Sens.* **2012**, *4*, 3501–3527.
5. Vågen, T.G.; Winowiecki, L.A.; Tondoh, J.E.; Desta, L.T.; Gumbricht, T. Mapping of soil properties and land degradation risk in Africa using MODIS reflectance. *Geoderma* **2016**, *263*, 216–225. [CrossRef]
6. Göttsche, F.M.; Hulley, G.C. Validation of six satellite-retrieved land surface emissivity products over two land cover types in a hyper-arid region. *Remote Sens. Environ.* **2012**, *124*, 149–158. [CrossRef]
7. Bellini, E.; Moriondo, M.; Dibari, C.; Leolini, L.; Staglianò, N.; Stendardi, L.; Filippa, G.; Galvagno, M.; Argenti, G. Impacts of Climate Change on European Grassland Phenology: A 20-Year Analysis of MODIS Satellite Data. *Remote Sens.* **2022**, *15*, 218. [CrossRef]
8. Wang, Y.; Liu, J.; Zhu, W. Estimation of Instantaneous Air Temperature under All-Weather Conditions Based on MODIS Products in North and Southwest China. *Remote Sens.* **2023**, *15*, 2701. [CrossRef]
9. Qi, Y.; Zhong, L.; Ma, Y.; Fu, Y.; Wang, X.; Li, P. Estimation of Land Surface Temperature Over the Tibetan Plateau Based on Sentinel-3 SLSTR Data. *IEEE J. Sel. Top. Appl. Earth Obs. Remote Sens.* **2023**, *16*, 4180–4194. [CrossRef]

10. Li, H.; Li, R.; Yang, Y.; Cao, B.; Bian, Z.; Hu, T.; Du, Y.; Sun, L.; Liu, Q. Temperature-Based and Radiance-Based Validation of the Collection 6 MYD11 and MYD21 Land Surface Temperature Products Over Barren Surfaces in Northwestern China. *IEEE Trans. Geosci. Remote Sens.* **2021**, *59*, 1794–1807. [CrossRef]
11. Erb, A.M.; Li, Z.; Sun, Q.; Paynter, I.; Wang, Z.; Schaaf, C. Evaluation of the Landsat-8 Albedo Product across the Circumpolar Domain. *Remote Sens.* **2022**, *14*, 5320. [CrossRef]
12. Hulley, G.C. NASA's MODIS/VIIRS Land Surface Temperature and Emissivity Products: Asssessment of Accuracy, Continuity and Science Uses. In Proceedings of the Agu Fall Meeting, New Orleans, LA, USA, 11–15 December 2017.
13. Zikan, K.H.; Adolph, A.C.; Brown, W.P.; Fausto, R.S. Comparison of MODIS surface temperatures to in situ measurements on the Greenland Ice Sheet from 2014 to 2017. *J. Glaciol.* **2022**, *69*, 129–140. [CrossRef]
14. Fréville, H.; Brun, E.; Picard, G.; Tatarinova, N.; Arnaud, L.; Lanconelli, C.; Reijmer, C.; van den Broeke, M. Using MODIS land surface temperatures and the Crocus snow model to understand the warm bias of ERA-Interim reanalyses at the surface in Antarctica. *Cryosphere* **2014**, *8*, 1361–1373. [CrossRef]
15. Hulley, G.C.; Hook, S.J. Intercomparison of versions 4, 4.1 and 5 of the MODIS Land Surface Temperature and Emissivity products and validation with laboratory measurements of sand samples from the Namib desert, Namibia. *Remote Sens. Environ.* **2009**, *113*, 1313–1318. [CrossRef]
16. Li, J.; Zhao, H.; Gu, X.; Yang, L.; Bai, B.; Jia, G.; Li, Z. Analysis of Space-Based Observed Infrared Characteristics of Aircraft in the Air. *Remote Sens.* **2023**, *15*, 535. [CrossRef]
17. Dong, L.; Tang, S.; Wang, F.; Cosh, M.; Li, X.; Min, M. Inversion and Validation of FY-4A Official Land Surface Temperature Product. *Remote Sens.* **2023**, *15*, 2437. [CrossRef]
18. Wu, X.; Yuan, J.; Wei, T.; Zhang, Y.; Wu, K.; Xia, H. Variation of Aerosol Optical Depth Measured by Sun Photometer at a Rural Site near Beijing during the 2017–2019 Period. *Remote Sens.* **2022**, *14*, 2908. [CrossRef]
19. Russell, B.J.; Soffer, R.J.; Ientilucci, E.J.; Kuester, M.A.; Conran, D.N.; Arroyo-Mora, J.P.; Ochoa, T.; Durell, C.; Holt, J. The Ground to Space CALibration Experiment (G-SCALE): Simultaneous Validation of UAV, Airborne, and Satellite Imagers for Earth Observation Using Specular Targets. *Remote Sens.* **2023**, *15*, 294. [CrossRef]
20. Yang, Z.; Gong, C.; Ji, T.; Hu, Y.; Li, L. Water Quality Retrieval from ZY1-02D Hyperspectral Imagery in Urban Water Bodies and Comparison with Sentinel-2. *Remote Sens.* **2022**, *14*, 5029. [CrossRef]
21. Soffer, R.J.; Ifimov, G.; Arroyo-Mora, J.P.; Kalacska, M. Validation of Airborne Hyperspectral Imagery from Laboratory Panel Characterization to Image Quality Assessment: Implications for an Arctic Peatland Surrogate Simulation Site. *Can. J. Remote Sens.* **2019**, *45*, 476–508. [CrossRef]
22. Kalacska, M.; Arroyo-Mora, J.P.; Soffer, R.; Leblanc, G. Quality Control Assessment of the Mission Airborne Carbon 13 (MAC-13) Hyperspectral Imagery from Costa Rica. *Can. J. Remote Sens.* **2016**, *42*, 85–105. [CrossRef]
23. Eon, R.; Gerace, A.; Falcon, L.; Poole, E.; Kleynhans, T.; Raqueño, N.; Bauch, T. Validation of Landsat-9 and Landsat-8 Surface Temperature and Reflectance during the Underfly Event. *Remote Sens.* **2023**, *15*, 3370. [CrossRef]
24. Gao, L.; Cao, L.; Zhong, Y.; Jia, Z. Field-Based High-Quality Emissivity Spectra Measurement Using a Fourier Transform Thermal Infrared Hyperspectral Imager. *Remote Sens.* **2021**, *13*, 4453. [CrossRef]
25. Wang, N.; Qian, Y.G.; Ma, L.L.; Tang, L.; Li, C. Influence of sensor spectral properties on temperature and emissivity separation for hyperspectral thermal infrared data. In Proceedings of the Workshop on Hyperspectral Image & Signal Processing: Evolution in Remote Sensing, Los Angeles, CA, USA, 21–24 August 2016.
26. Shao, H.; Liu, C.; Xie, F.; Li, C.; Wang, J. Noise-Sensitivity Analysis and Improvement of Automatic Retrieval of Temperature and Emissivity Using Spectral Smoothness. *Remote Sens.* **2020**, *12*, 2295. [CrossRef]
27. Shao, H.; Liu, C.; Li, C.; Wang, J.; Xie, F. Temperature and Emissivity Inversion Accuracy of Spectral Parameter Changes and Noise of Hyperspectral Thermal Infrared Imaging Spectrometers. *Sensors* **2020**, *20*, 2109. [CrossRef] [PubMed]
28. Kim, S.; Shin, J.; Kim, S. AT2ES: Simultaneous Atmospheric Transmittance-Temperature-Emissivity Separation Using Online Upper Midwave Infrared Hyperspectral Images. *Remote Sens.* **2021**, *13*, 1249. [CrossRef]
29. Sidhu, N.; Pebesma, E.; Wang, Y.-C. Usability Study to Assess the IGBP Land Cover Classification for Singapore. *Remote Sens.* **2017**, *9*, 1075. [CrossRef]
30. Xu, Y.; Chen, X.; Liu, M.; Wang, J.; Zhang, F.; Cui, J.; Zhou, H. Spatial–Temporal Relationship Study between NWP PWV and Precipitation: A Case Study of 'July 20' Heavy Rainstorm in Zhengzhou. *Remote Sens.* **2022**, *14*, 3636. [CrossRef]
31. Jin, R.; Li, X.; Liu, S.M. Understanding the Heterogeneity of Soil Moisture and Evapotranspiration Using Multiscale Observations from Satellites, Airborne Sensors, and a Ground-Based Observation Matrix. *IEEE Geosci. Remote Sens. Lett.* **2017**, *14*, 2132–2136. [CrossRef]
32. Zhu, W.; You, D.; Wen, J.; Tang, Y.; Gong, B.; Han, Y. Evaluation of Linear Kernel-Driven BRDF Models over Snow-Free Rugged Terrain. *Remote Sens.* **2023**, *15*, 786. [CrossRef]
33. Roujean, J.L.; Leroy, M.; Deschamps, P.Y. A bidirectional reflectance model of the Earth's surface for the correction of remote sensing data. *J. Geophys. Res. Atmos.* **1992**, *972*, 20455–20468. [CrossRef]
34. Lucht, W. Expected retrieval accuracies of bidirectional reflectance and albedo from EOS-MODIS and MISR angular sampling. *J. Geophys. Res. Atmos.* **1998**, *103*, 8763–8778. [CrossRef]

35. Mira, M.; Weiss, M.; Baret, F.; Courault, D.; Hagolle, O.; Gallego-Elvira, B.; Olioso, A. The MODIS (collection V006) BRDF/albedo product MCD43D: Temporal course evaluated over agricultural landscape. *Remote Sens. Environ.* **2015**, *170*, 216–228. [CrossRef]
36. Robitaille, P.M.; Crothers, S.J. Universality and Kirchhoff's Law of Thermal Emission. In Proceedings of the APS April Meeting 2015, Baltimore, MD, USA, 11–14 April 2015.